Modeling of thermal and lattice misfit stresses within a thermal barrier coating

Hani Abu El Hawa, Abir Bhattacharyya, and David Maurice

U.S. Department of Energy, National Energy Technology Laboratory,
1450 Queen Ave SW, Albany, OR 97321, USA

ABSTRACT

An analytical model was developed to determine the stress distribution over thickness for a multilayered Thermal Barrier Coating (TBC) system deposited within a cylindrical reaction vessel. Temperature dependent material properties were used to estimate the stress values. It was found that, even for small lattice misfits, very high compressive elastic stresses could exist at the ceramic-bond coat interface immediately after deposition. Furthermore, this interfacial stress could ultimately relax to a lower value with increasing film thickness by dislocation nucleation. In the presence of a Thermally Grown Oxide (TGO), however, a tensile stress was generated within the oxide layer and discrete changes in stress profile were predicted at ceramic-TGO and TGO-bond coat interfaces. While the stress-change was higher at the ceramic-TGO interface for a high deposition temperature, the change was greater at the TGO-bond coat interface at a lower deposition temperature. A high compressive stress was predicted within the TGO layer upon cooling down the TBC system to room temperature and the stress-change was highest at the TGO-bond coat interface. Finally, when the TGO layer was subjected to fatigue loading under compressive mean stress during thermal cycling, the model predicted that the internal pressure of the cylindrical vessel reduces the magnitude of mean stress and increases the stress-range in the thermal stress cycle. The effects of evolved stresses on the context of interfacial failure of TBCs should provide fundamental insight into material selection and component design.

KEY WORDS

Thermal Barrier Coating, Residual Stress, Lattice Misfit, Thermal Mismatch, Ceramic-Metal Interface, Hetero-epitaxy; Misfit Dislocations.

1. INTRODUCTION

Thermal Barrier Coatings (TBCs) are widely used to protect metallic components from harsh service conditions [1-4]. A typical TBC system consists of three layers; (i) a top coat, (ii) a bond coat (which also serves as an environmental barrier layer between the top coat and the metallic component/substrate) and (iii) a metallic substrate. The top coat is typically a ceramic based material, which provides thermal insulation to the substrate [5]. A desired top coat is expected to have several properties such as a high melting point, low thermal conductivity, chemical inertness, a low thermal expansion coefficient and the ability to resist phase transformations during thermal cycling [5, 6]. The bond coat layer provides protection against the oxidation of the substrate by forming a Thermally Grown Oxide (TGO). This layer forms during high temperature operations in the presence of air and/or moisture and typically have thickness between 1μm-10 μm [7-9].

The thickness of a typical top coat used in gas turbine engine blades, for example, ranges between 100-250 μm. The turbine blades contain cooling channels to reduce the temperature of the Ni-based substrates during operation. Therefore a 100-250 μm thick TBC can effectively reduce the temperature to the acceptable limit for the Ni-based super alloys in turbine blades [10-13]. Thicker coatings (> 500-2000 μm), however, may be necessary for other components operating at higher temperatures, which may not have an engineered system for cooling. TBCs are usually subjected to a variety of environmental conditions such as thermal cycling, pressure cycling, abrasive wear, and/or corrosion [14-17]. As a result, residual stresses evolve within the TBC layers and eventually the TBC fails by either rupturing of the top coat or TGO layer. or by delamination at either the top coat/TGO or TGO/bond coat interface.

There are multiple sources of residual stresses in a TBC system after deposition. First, the quenching of molten particles upon contact with the substrate results in tensile stresses in the top layer and corresponding compressive stresses in the substrate. However, several relaxation mechanisms such as microcracking in ceramics, and creep in metallic bond coats, etc. reduce the quench stress to a low value [18, 19]. Second, stresses arise due to the thermal mismatch between the top coat and the bond coat [20]. When a TBC system is cooled down from a deposition temperature to room temperature, the mismatch in the coefficients of thermal expansion (CTE) of the ceramic top coat and the metallic bond coat layer underneath it leads to the generation of additional residual stresses within each layer and at the interfaces. Third, the lattice misfit among the TBC layers and the substrate can also contribute to the interfacial stresses [21, 22]. Furthermore, the formation of new phases can impact the lattice misfit stresses. For example, the formation of a TGO layer can lead to the generation of additional interfacial stresses. These residual stresses can initiate micro-cracks at the bond coat/TGO/top coat interfaces which lead to the interface debonding [23].

Several analytical models have been developed to evaluate the residual stress profiles during TBC deposition and component operation under a variety of conditions [20, 24-27]. Those studies consider the thermal mismatch as the major contributor to the stresses within the TBC layers. The effect of lattice misfit on the stress profile within the TBC layers has not been previously reported. The lattice misfit can contribute to additional stresses in individual TBC layers or may introduce additional defects at the interfaces. Additionally, any effect of phase transformation or evolution of new phases or compounds (e.g. TGO) during the deposition or operation of TBC involves change in lattice parameter between parent and nucleating phases and essentially induces lattice misfit. In a companion paper [28], we utilize the principle of elastic strain energy minimization to model the impacts of lattice misfits on interfacial coherency. The goal of that paper is to evaluate the role of lattice misfit on the evolution of coherency strain and defects at the interface to predict the failure of the top coat and interfacial delamination in TBC systems. The results of these modeling efforts enable the prediction of both stresses and defect generation, and we draw on the findings of that paper in this work. Moreover, most of the studies on thermal stress evolution within TBCs were performed on flat substrate- thin film systems. Therefore, an analysis of the effects of thermal mismatch and lattice misfit on the evolution of stresses within a cylindrical TBC system subjected to both temperature and pressure is of practical importance for materials and component design, many of which have cylindrical geometries and are operated at high temperature conditions.

The goal of the current work is to develop an analytical model for predicting the stress profile within a TBC system deposited inside a cylindrical reaction vessel, and analyze its structural integrity during operation under a high temperature and pressure environment. In this study, we consider a cylindrical pressure vessel containing layers typical of a TBC. An analytical mathematical model based on the Lame's theory [29] of stresses within a cylindrical pressure vessel is developed to evaluate radial and circumferential stresses evolution at the interface between two adjacent materials layers. In this model we have incorporated the effects of thermal mismatch strain and lattice misfit strain to the stress and defect evolution at the interfaces. We have demonstrated the influence of lattice misfit induced stresses on the characteristics of the interfaces between TBC layers and on interfacial adhesion. An intermediate TGO layer is incorporated between the top coat and the bond coat to assess the effect of the TGO on the residual stress evolution during heating and cooling. The effects of evolved stresses on the context of interfacial failure of TBCs should provide fundamental insight into material selection and component design.

2. MODEL DEVELOPMENT

A schematic of a cylindrical pressure vessel type TBC system subjected to an internal pressure p_0 is shown in Fig. 1. Here E_i, a_i, α_i, ν_i and r_i represent Young's modulus, lattice constant, coefficient of thermal expansion, Poisson's ratio and radius for layer *i*, respectively, with *i* = 1-4 for the top coat, thermally grown oxide, bond coat and substrate layers, respectively.

The radially acting interfacial stress at each boundary between two successive layers is represented by p_i (*i* = 1-3). The internal pressure p_0 was arbitrarily set to 7.0 MPa, as this is typical of a pressure vessel, a representative use of such a materials structure. The external pressure (p_4), at the outside of the vessel is considered zero gauge.

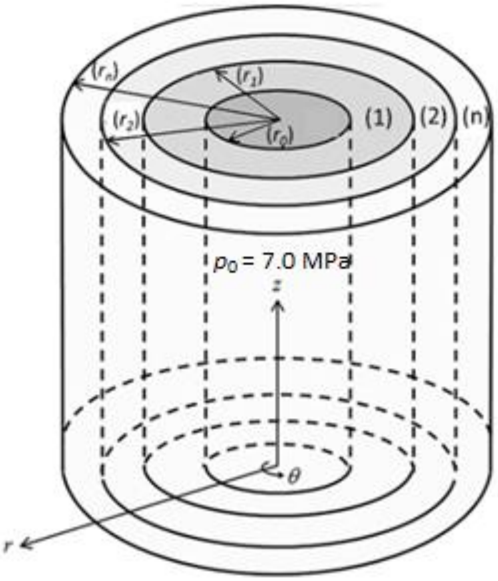

Figure 1 (a) Illustration of a laminated TBC system components in the form of a cylindrical pressure vessel. Each layer may be a unique material with distinct properties. The internal

pressure p_0 = 7.0 MPa while p_4 which is at the outside surface was always set to zero gauge. p_i is the internal pressure at the outside radius of layer *i* (at the interface between layer *i* and *i+1*). The internal radius of the pressure vessel is r_0 = 1 m.

For a symmetrical *2D* cylindrical geometry, the governing equations for equilibrium can be described as [29]:

$$\frac{\partial \sigma_r}{\partial r}+\frac{1}{r}\frac{\partial \tau_{r\theta}}{\partial \theta}+\frac{\sigma_r-\sigma_\theta}{r}+R=0 \tag{1}$$

$$\frac{\partial \tau_{r\theta}}{\partial r}+\frac{1}{r}\frac{\partial \sigma_\theta}{\partial \theta}+\frac{2\tau_{r\theta}}{r}+R=0$$

Where σ_r and σ_θ are the radial and circumferential stresses, respectively. Due to the axi-symmetry of the cylindrical geometry, the shear stress $\tau_{r\theta}$ is set to zero and the stress components are functions of *r* only. *R*, which is the rotation term, is set to zero.

Hence equations (1) become:

$$\frac{d\sigma_r}{dr}+\frac{\sigma_r-\sigma_\theta}{r}=0 \tag{2}$$

The above equation can be solved analytically to yield the following general solutions:

$$\sigma_r(r)=C_1+\frac{C_2}{r^2} \tag{3}$$

$$\sigma_\theta(r)=C_1-\frac{C_2}{r^2} \tag{4}$$

Where *C₁* and *C₂* are constants, which can be determined by imposing appropriate boundary conditions (Fig. 1).

For layer 1 ($r_0 \le r \le r_1$);

$$\sigma_r=-p_0 \quad \text{at } r=r_0 \tag{5}$$

$$\sigma_r=-p_1 \quad \text{at } r=r_1$$

For layer 2 ($r_1 \le r \le r_2$);

$$\sigma_r=-p_1 \quad \text{at } r=r_1 \tag{6}$$

$$\sigma_r=-p_2 \quad \text{at } r=r_2$$

For layer 3 ($r_2 \le r \le r_3$);

$$\sigma_r=-p_2 \quad \text{at } r=r_2 \tag{7}$$

$$\sigma_r = -p_3 \qquad \text{at } r = r_3$$

For layer 4 ($r_3 \le r \le r_4$);

$$\sigma_r = -p_3 \qquad \text{at } r = r_3 \tag{8}$$

$$\sigma_r = 0 \qquad \text{at } r = r_4$$

By imposing the above boundary conditions, the following solutions for the radial and circumferential stresses as functions of *r* were obtained for each layer:

For the top coat, $r_0 \le r \le r_1$;

$$\sigma_{1,r}(r) = \frac{p_0 r_0^2 - p_1 r_1^2}{r_1^2 - r_0^2} - \frac{r_0^2 r_1^2 (p_0 - p_1)}{r^2 (r_1^2 - r_0^2)} \tag{9}$$

$$\sigma_{1,\theta}(r) = \frac{p_0 r_0^2 - p_1 r_1^2}{r_1^2 - r_0^2} + \frac{r_0^2 r_1^2 (p_0 - p_1)}{r^2 (r_1^2 - r_0^2)}$$

For the TGO layer, $r_1 \le r \le r_2$;

$$\sigma_{2,r}(r) = \frac{p_1 r_1^2 - p_2 r_2^2}{r_2^2 - r_1^2} - \frac{r_1^2 r_2^2 (p_1 - p_0)}{r^2 (r_2^2 - r_1^2)} \tag{10}$$

$$\sigma_{2,\theta}(r) = \frac{p_1 r_1^2 - p_2 r_2^2}{r_2^2 - r_1^2} + \frac{r_1^2 r_2^2 (p_1 - p_2)}{r^2 (r_2^2 - r_1^2)}$$

For the bond coat, $r_2 \le r \le r_3$;

$$\sigma_{3,r}(r) = \frac{p_2 r_2^2 - p_3 r_3^2}{r_3^2 - r_2^2} - \frac{r_2^2 r_3^2 (p_2 - p_3)}{r^2 (r_3^2 - r_2^2)} \tag{11}$$

$$\sigma_{3,\theta}(r) = \frac{p_2 r_2^2 - p_3 r_3^2}{r_3^2 - r_2^2} + \frac{r_2^2 r_3^2 (p_2 - p_3)}{r^2 (r_3^2 - r_2^2)}$$

For the substrate, $r_3 \le r \le r_4$;

$$\sigma_{4,r}(r) = \frac{p_3 r_3^2}{r_4^2 - r_3^2}\left(1 - \frac{r_4^2}{r^2}\right) \tag{12}$$

$$\sigma_{4,\theta}(r) = \frac{p_3 r_3^2}{r_4^2 - r_3^2}\left(1 + \frac{r_4^2}{r^2}\right)$$

To maintain the continuity of the interfaces between two successive layers, the radial displacement of two successive layers should be same. This can be expressed in terms of the continuity of the circumferential strain as follows [29]:

$$\varepsilon_{i,\theta} = \varepsilon_{i+1,\theta}\ , \text{ where } i = 1, 2, 3 \tag{13}$$

Where ε_θ is the circumferential strain and can be expressed for a given layer *i* as follows [27]:

$$\varepsilon_{i,\theta} = \frac{\sigma_{i,\theta} - \upsilon_i \sigma_{i,r}}{E_i} \tag{14}$$

The circumferential strain is influenced by the mismatch in thermal expansion coefficients between the layers. A mismatch in the lattice parameters between two successive material layers can also result in strain at their interface. Similarly, a quenching-induced strain component exists at individual layers. The effects of the thermal mismatch, lattice misfit and quenching induced strains are incorporated in the model by including a thermal strain component in Eq. (15). The resulting circumferential strain ($\varepsilon_{i,\theta}$) component for a given layer is then expressed as:

$$\varepsilon_{i,\theta} = \frac{\sigma_{i,\theta} - \upsilon_i \sigma_{i,r}}{E_i} + \alpha_i \Delta T + \varepsilon_{m_i} + \varepsilon_{q_i} \tag{15}$$

Where ΔT is the difference between the final temperature (T_f) and the initial temperature (T_i) during thermal cycling, i.e. $\Delta T = T_f - T_i$, ε_{m_i} is the mean lattice misfit strain between two successive material layers at an interface *i*, and *i*+1, and ε_{q_i} is the quench induced strain in layer *i* expressed as $\varepsilon_{q_i} = \alpha_i (T_m - T_s)$, where T_m and T_s are the melting point of the coating material, and the deposition temperature, respectively.

By imposing the continuity of circumferential strain condition at the interface, the following expressions were obtained for the interfacial stresses p_1, p_2 and p_3 :

$$\begin{gathered}
p_1 = \frac{\varepsilon_{m_1} + \varepsilon_{q_1} + (\alpha_2 - \alpha_1)\Delta T - 2\left(\dfrac{p_0 r_0^2}{E_1 (r_1^2 - r_0^2)} + \dfrac{p_2 r_2^2}{E_2 (r_2^2 - r_1^2)}\right)}{\dfrac{r_1^2(\upsilon_1 - 1) - r_0^2(\upsilon_1 + 1)}{E_1 (r_1^2 - r_0^2)} + \dfrac{r_1^2(\upsilon_2 - 1) - r_2^2(\upsilon_2 + 1)}{E_2 (r_2^2 - r_1^2)}} \\
p_2 = \frac{\varepsilon_{m_2} + \varepsilon_{q_2} + (\alpha_3 - \alpha_2)\Delta T - 2\left(\dfrac{p_1 r_1^2}{E_2 (r_2^2 - r_1^2)} + \dfrac{p_3 r_3^2}{E_3 (r_3^2 - r_2^2)}\right)}{\dfrac{r_2^2(\upsilon_2 - 1) - r_1^2(\upsilon_2 + 1)}{E_2 (r_2^2 - r_1^2)} + \dfrac{r_2^2(\upsilon_3 - 1) - r_3^2(\upsilon_3 + 1)}{E_3 (r_3^2 - r_2^2)}} \\
p_3 = \frac{\varepsilon_{m_3} + \varepsilon_{q_3} + (\alpha_4 - \alpha_3)\Delta T - \dfrac{2 p_2 r_2^2}{E_3 (r_3^2 - r_2^2)}}{\dfrac{r_3^2(\upsilon_3 - 1) - r_2^2(\upsilon_3 + 1)}{E_3 (r_3^2 - r_2^2)} + \dfrac{r_3^2(\upsilon_4 - 1) - r_4^2(\upsilon_4 + 1)}{E_4 (r_4^2 - r_3^2)}}
\end{gathered} \tag{16}$$

The contributions of thermal mismatch, lattice misfit and quenching strains are incorporated in Eq. (16). The above set of equations can be solved simultaneously to obtain explicit values of p_1, p_2 and p_3 for a given set of conditions. While Eqs. (16) are not explicitly written as such, the model described does incorporate the temperature dependence of the materials properties which were determined by interpolation as will be described in the section to follow.

3. MATERIALS SELECTION AND PROPERTIES

Materials for a representative TBC system were selected to evaluate the model described in section 2. Inconel alloys are typically used for high-temperature applications such as furnace tubes, turbine blades, heat shields, etc. [30]. Inconel 738 was used as the substrate or base material of the vessel for model testing. Alloys of the form MCrAlY are frequently used as bond coat materials due to their high oxidation resistance [31]. For testing this model NiCoCrAlY as the bond coat material and Yttria stabilized zirconia (YSZ), as the top coat were chosen. The TGO layer between the top coat and the bond coat is assumed to be α-Al_2O_3 which forms due to the oxidation of the bond coat. Temperature dependent physical and mechanical properties of each layer along with their thicknesses used in the model are provided in Table 1. Linear interpolation was used to estimate properties at temperatures other than those listed in the table. This configuration of materials and thicknesses was selected to illustrate the model. The TBC system described, and the specific model predictions, are not suggested to be universal to all TBC systems or applications.

Table 1 Temperature dependent physical/mechanical properties of TBC components used in the model. The properties were taken from [15] and [32] except lattice parameters, which were extracted from [33-36].

Layer	Thickness	T (°C)	*E* (GPa)	*v*	α (10^{-6} K^{-1})	λ (W/m^2K)	*a* (°A)
Top Coat (TC) 8 mol% YSZ (1)	2 mm	20	204	0.10	9.68	1.20	5.12
		800	179	0.11	9.88	1.16	
		1000	186	0.12	10.34	1.14	
Thermally Grown Oxide (TGO) α-Al_2O_3 (2)	0-10 μm	20	400	0.23	8.00	10.00	4.75
		800	355	0.25	9.00	4.40	
		1000	325	0.25	9.30	4.40	
Bond Coat (BC) NiCoCrAlY (3)	200 μm	20	200	0.30	12.5	5.80	3.60
		800	145	0.32	14.3	14.5	
		1000	120	0.33	16.0	16.2	
Substrate Inconel 738 (4)	76.2 mm	20	204	0.32	12.6	11.50	3.59
		800	161	0.34	15.4	26.63	
		1000	137	0.34	16.3	33.08	

4. RESULTS AND DISCUSSION

The top coat, bond coat and substrate materials have different lattice parameters and Coefficients of Thermal Expansion (CTE) which can result in lattice misfit and thermal mismatch between the layers. As illustrated in Table 1, these differences can be significant. It is therefore necessary to investigate the effects of lattice misfit, and thermal mismatch on the interfacial strain and stress. We began analyzing this problem with three initial layers: top coat; bond coat; and substrate, and determine the stress profile upon cooling from an elevated temperature such as might occur after TBC deposition. Then a 10 µm thick TGO layer was incorporated between the bond coat and the top coat at a constant operating temperature and pressure, and the subsequent change in the stress profiles were determined. Finally, thermal cycling was simulated with the TGO layer present to observe any changes in the stress profiles.

4.1 Lattice misfit, interfacial strain and misfit dislocations

To account for the stress arising from the lattice parameter misfit at the interface between two adjacent layers, a mean strain ($\varepsilon_{m\,\mathrm{i}}$) was added to Eq. (15). The lattice misfit is expressed as [22]:

$$f = \frac{a_f - a_s}{a_s} \tag{17}$$

Where a_s and a_f are the lattice parameters of the substrate and the film, respectively.

An interface can be coherent, semi-coherent or incoherent depending upon the lattice misfit at the interface. Coherent interfaces typically form when the lattice misfits are < ±10% [37]. Semi-coherent interfaces form for a lattice misfit between 10-20% during hetero-epitaxial growth of a material having a different crystal structure and bonding characteristics (e.g. metal and ceramic) [37]. The high mismatch cannot be accommodated by elastic strain alone at the lattices at the interface. Consequently, dislocations form at the interface to relieve the strain due to misfit. Beyond 20% misfit results in the formation of an incoherent interface [37] and thus 20% can be considered as a practical limit of the lattice misfit (f) contributing to the strain at the interface [37]. For a full or partial epitaxy, the lattices within the film and the substrate at the vicinity of a coherent or semi-coherent interface will orient themselves to reduce the lattice misfit (f) to less than 20%.

In a companion paper [28], we utilized the principle of elastic strain energy minimization to model the impacts of lattice misfits on interfacial coherency. The salient findings of this effort are encapsulated as follows.

For an epitaxial growth in a given substrate-film system, a limiting misfit (f^{Lim}) for the coherent interface can be defined beyond which a semi-coherent interface will form. Accordingly, a mean strain ($|\varepsilon_m| \leq |f|$) at the interface of a film-substrate system can be defined as:

$$\varepsilon_m = \begin{cases} -f & \text{for } f \le f^{Lim} \\ -\left(f + \dfrac{b}{p}\right) = -\left(\dfrac{a_f - a_s}{a_s} + \dfrac{b}{p}\right) & \text{for } f > f^{Lim} \end{cases} \tag{18}$$

Where b is the Burgers vector component of a dislocation and p is the mean spacing between the dislocations in a square array of dislocations. The dislocations relieve the lattice misfit (f) and therefore b/p always has opposite sign to f . Eq. (18) suggests that a positive f results in negative mean strain (ε_m) and vice versa. The mean spacing p is directly related to the dislocation density (N) by $N = 1/p^2$ [38, 39].

Eq. (18) suggests that dislocations nucleate at the interface when the lattice misfit, $f > f^{Lim}$. The signs of f and b/p will always be different as dislocations relieve the lattice misfit. As a result, the magnitude of mean strain will always be less than or equal to the lattice misfit, i.e. $|\varepsilon_m| \le |f|$. However, the magnitude and sign of ε_m depends on the relative magnitude and sign of f and b/p. The dislocation density (N) for a square array of 90° (edge) dislocations at the interface is defined as $N = 1/p^2$. Determination of p is therefore necessary to calculate the equilibrium dislocation density and the remaining strain at the interface. For small lattice misfits, the dislocation nucleation may become unfavorable when the film thickness is small resulting in a coherent interface. Dislocation nucleation is favorable at greater film thicknesses and for higher lattice misfits. A methodology to determine the range of lattice misfits for each type of interface and the stress state at the interfaces is provided in the same companion paper [28].

The stress state and the types of interface depends on the macroscopic failure strength and Burgers vector of the film and the equilibrium dislocation density at the interface. The following interfaces may exist between dissimilar materials;

> ***Case (i):*** An incoherent interface or a highly disordered (amorphous) region is expected to form for a very high lattice misfit or a high lattice commensurability ratio, CR (defined as the integral multiples of lattice parameter or interplanar spacing required to match at the interface) at an interface [36, 37].
>
> ***Case (ii)*****:** A weakly stressed semi-coherent interface with a high density of misfit dislocations. For a Ni-cubic YSZ substrate-film system, a semi-coherent interface may exist for the lattice misfit range, $-0.0986 \le f \le -0.0203$ and $0.0146 \le f \le 0.0228$ [28].
>
> ***Case (iii)*****:** A dislocation-free stressed coherent interface. For a Ni-cubic YSZ substrate-film system, semi-coherent interface may exist for the lattice misfit range, $-0.0146 \le f \le -0.0012$ [28].

Any of the abovementioned cases can exist at an interface between the layers of a TBC system. Cases (ii) and (iii) are especially interesting for the hetero-epitaxial growth of ceramics on a metallic substrate. Based on the magnitude of the lattice misfit, either a stressed coherent interface or a relaxed semi-coherent interface with a high defect concentration might exist. The stresses and/or the defects can reduce the adhesion of the layers at the interface.

Table 2 provides representative, empirically determined orientation relationships, some of which were used in subsequent modeling sections. The data is in reasonable agreement with our estimated lattice misfits and will be used in our calculations.

Table 2 Representative orientation relationships (OR-s) for interfaces between c-YSZ-Ni as reported in literature. The same OR-s are considered to estimate the lattice misfits between c-YSZ and NiCoCrAlY bond coat in this study.

Interface Types	Orientation Relationship (OR)	Commensurability Ratio (CR)	Misfit (*f*)	References
Incoherent (case i)	$(111)_{c-YSZ} \parallel (111)_{MCrAlY}$ $[1\bar{1}0]_{c-YSZ} \parallel [1\bar{1}0]_{MCrAlY}$	1:1	0.42	Sasaki *et al.* [40]
Semi-coherent (case ii)	$(111)_{c-YSZ} \parallel (111)_{MCrAlY}$ $[2\bar{1}\bar{1}]_{c-YSZ} \parallel [0\bar{1}1]_{MCrAlY}$	5:4	0.026	Christensen *et al.* [41]
Coherent (case iii)	$(001)_{c-YSZ} \parallel (001)_{\mathrm{MCrAlY}}$ $[010]_{c-YSZ} \parallel [111]_{\mathrm{MCrAlY}}$	1:2	0.0057	Sasaki *et al.* [40]

Among these three cases listed in Table 2, we applied our model for only two representative cases and determined the corresponding stress profiles for a defect free coherent interface with lattice misfit strain of -0.0057 (f = 0.0057 case (iii)) and for a highly defected semi-coherent interface with f = 0.026 (case (ii)) with no remaining strain due to lattice misfit. A similar approach can be used for other cases.

4.2 Lattice misfit after formation of a TGO

A TGO layer of rhombohedral α-Al_2O_3 forms between the YSZ top coat and the Ni-based bond coat during high-temperature operation of the TBCs. Consequently, lattice misfits will exist at the interface between c-YSZ and α-Al_2O_3 and between α-Al_2O_3 and NiCoCrAlY. The best match at the interface is possible between the (111) plane of a cubic crystal and (0001) plane of a rhombohedral crystal due to three-fold symmetry of (111) plane and six-fold symmetry of the (0001) [36]. The representative orientation relationships for the YSZ-α Al_2O_3-NiCoCrAlY system are listed in Table 3 along with the corresponding lattice misfits calculated based on the procedure described in section 4.1.

Table 3 Representative orientation relationships (OR-s) for the interfaces between c-YSZ –α Al_2O_3- Ni

Interface types	Orientation Relationship (OR)	Commensurability Ratio (CR)	Misfit (*f*)	References
Semi-coherent (case (ii)) or Incoherent (case (i))	$(111)_{c-YSZ} \parallel (0001)_{Al_2O_3}$ $[\bar{1}10]_{c-YSZ} \parallel [\bar{1}100]_{Al_2O_3}$ or $[11\bar{2}]_{c-YSZ} \parallel [11\bar{2}0]_{Al_2O_3}$	1:1	0.14	Korte et al. [36]
		8:7	-0.0057	
Semi-coherent (case (ii)) or Incoherent (case (i))	$(0001)_{Al_2O_3} \parallel (111)_{MCrAlY}$ $[\bar{1}100]_{Al_2O_3} \parallel [\bar{1}10]_{MCrAlY}$ or $[11\bar{2}0]_{Al_2O_3} \parallel [11\bar{2}]_{MCrAlY}$	1:1	0.38	Zhang et al. [42]
		5:8	0.011	

If either a high lattice misfit or a high CR is present, the tendency is to form either a disordered (incoherent) or a semi-coherent interface. A partially stressed or stress-free semi-coherent interface with high defect densities therefore may exist between the top coat-TGO and TGO-bond coat (case ii). High dislocation densities reduces the adhesion of interfaces [43], rendering the interface prone to delamination if either the top coat or TGO thickness increases or if a crack reaches the interfaces.

4.3 Residual stress profiles

4.3.1 Quench stresses

Only three layers, namely the YSZ top coat, Ni-based MCrAlY bond coat and Inconel substrate were considered initially (i.e. the TGO thickness was set to zero). As described in section 2, the quenching induced strain is expressed as $\varepsilon_{q_i} = \alpha_i (T_m - T_s)$. As diffusive stress relaxation by creep is activated at high temperatures, the T_m in the equation is replaced by a lower creep initiation temperature ($\sim 0.5T_m$) for the calculation of quench stresses. Based on T_m= 2,700°C for cubic YSZ, the stress profile due to quenching of molten ceramic on the substrate layers at a deposition temperature of 1,200°C is plotted using Eqs. (9-12) and (16) and the plots are shown in Fig. 2.

Such a deposition temperature is typical in Chemical Vapor Deposition (CVD) [44, 45] and is at the high end of the Electron Beam Physical Vapor Deposition (EBPVD) techniques [46, 47].

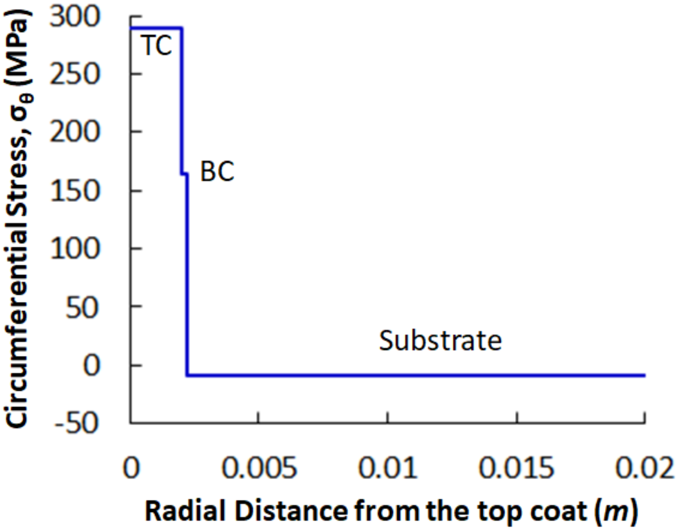

Figure 2 Quenching induced stresses before stress relaxation by microcracking and creep.

A high tensile quenching stress of ~290 MPa is predicted in the YSZ top coat (Fig. 2). At such a high stress level, the cubic YSZ will undergo microcracking due to its low tensile strength (tensile strength of 8 mol% cubic YSZ= 210 MPa [48]). Kuroda *et al.* [18, 19] showed that microcracking relaxes the quenching induced residual stresses in ceramics and that only a small quenching stress of <50 MPa remains in ceramics as a result. For metallic coatings during the deposition of bond coats, creep and plasticity act as major stress relaxation mechanisms and reduce the residual stress at high deposition temperatures**.** Furthermore, the residual stress for Ni coatings is typically less than 100 MPa at the low deposition temperature of 77°C, and the stress decreased to < 20 MPa at 727°C [18]. For all practical purposes, such small stresses can be neglected in comparison to the high magnitudes (several hundreds of MPa) of thermal and lattice misfit stresses. However, contrary to the general expectation based on the equation for quench strain, Kuroda's study revealed that the residual stress for a Ni-20Cr alloy initially increases with deposition temperature and then decreases to ~ 45 MPa at at 727°C. They proposed that a better adhesion between deposited and substrate layers at higher temperature provides a greater constraint to thermal contraction during quenching. Hence the stress increases with temperature until creep activates to relax the stress. This behavior is contrarian to that obtained from the equation for quenching stress, and cannot be modeled by bulk mechanical properties. Instead, the bonding condition between the splats needs to be considered. Our model differs in that it can be used to calculate the quench stresses based upon the bulk properties of materials. According to that model quench stresses vary with deposition temperature, such that at 1200°C, the quench stress will be greater than the tensile stress of YSZ. In this case microcracking would relax the stresses within the ceramic top coat, and the stress in the bond coat will be relaxed by creep. However, for higher deposition temperatures, the quench stress will be lower than the tensile strength of the ceramic, and therefore a relaxation via microcracking would not be expected.

The presence of dislocation free coherent interfaces with a misfit (f) value of 0.048 has been observed for cubic ZrO_2 film-FCC Fe substrate interface under transmission electron microscopy [49] . The presence of a dislocation free epitaxial interface with high lattice misfit of 0.074 in a YSZ film- $SrTiO_3$ substrate system was reported by Sillassen et al. [50]. These observations suggest that a finite mean strain due to lattice misfit can be present in the first few atomic layers of an interface. As a result, the interface will be stressed and should be accounted for in stress calculations. The evolution of stress that occur with increasing film thickness as will be discussed below.

To show the effect of lattice misfit at the interface, we have considered two cases of misfit during the initial early stage of the film deposition process (i.e. when film thickness is only a few atomic layers). In the first case, we assume a fully relaxed semi-coherent interface with a high lattice misfit, f = 0.026 (case (ii) in Table 2). For simplicity, we assume that the dislocation density at the interface is such that all the strain due to lattice misfit is relieved. The corresponding dislocation spacing based on Eq. (18) is $p = \frac{b}{f} = 13.92$ nm, which results in a dislocation density of $N = \frac{1}{p^2} \approx 5 \times 10^{15}$/m^2.

In the second case, we have assumed a small initial lattice misfit of 0.0057 (case (iii) in Table 2). As described fully in our companion paper [28], a fully coherent interface exists for this level of misfit when $h < 7\,nm$ and the lattice misfit induced stress can be significant while $h < 7\,nm$. The stress profile for the first case therefore considers only the effect of thermal mismatch and the second case considers the effects of both the thermal mismatch and the lattice misfit strain. In both cases, the stress profiles were plotted for an initial film thickness of 5 *nm* (Fig. 3(a) and 3(b)) to demonstrate the effects of lattice misfit on the coherency of an interface and the resulting mean strain in the film. The effect of film thickness on the stress profile is then explained and subsequently the stress profiles were plotted for a thicker film of 2 *mm*.

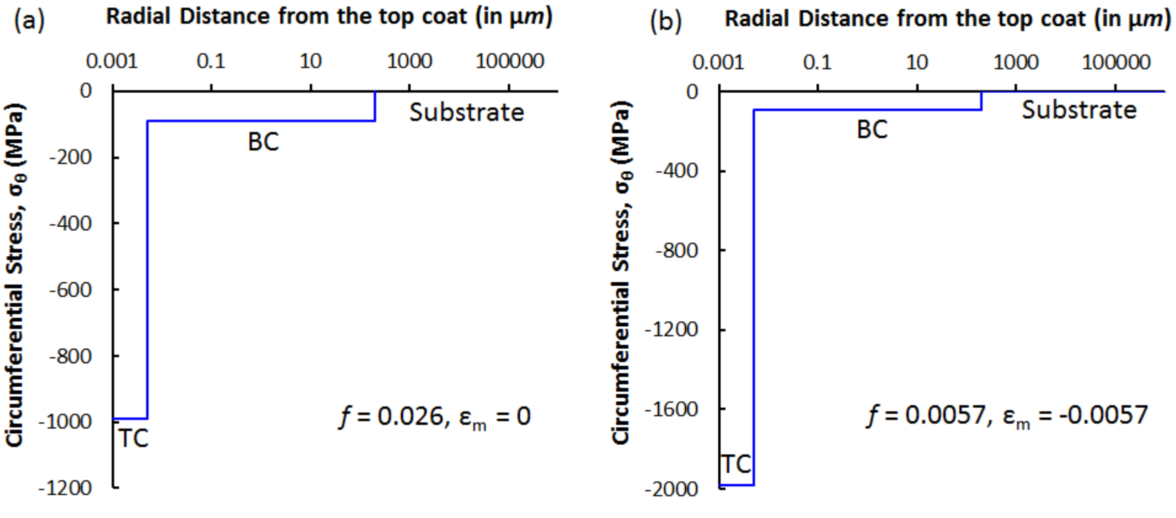

Figure 3 Circumferential stress profiles due to cooling of a TBC system from 1,200°C to 20°C during deposition (p_0 = 0 MPa gauge, no TGO) for (a) $f = 0.026$ and (b) $f = 0.0057$ between the top coat and Ni-based bond coat. The thickness of top coat = 5 nm. The mean strain at the

interface due to lattice misfit for $f = 0.026$ is zero, whereas the mean strain due to lattice misfit for $f = 0.0057$ is -0.0057. The TC and BC represents top coat and bond coat, respectively.

4.3.2 Residual stress after deposition

The lattice misfit between the bond coat and substrate was kept at 0.0028. The calculations for this initial state were performed for a 5 *nm* thick top coat and 0.2 mm thick bond coat. The internal pressure (p_0) was set to zero gauge. The circumferential stress distributions as a function of thickness of the TBC layers are shown in Fig. 3(a) and Fig. 3(b) for cooling down from a deposition temperature of 1,200°C to 20°C for mean misfit strain (ε_m) values of zero (case (ii)) and -0.0057 (case (iii)), respectively, arising due to lattice misfit between the top coat and the bond coat.

Our analysis reveals that the compressive radial stress (σ_r) is on the order of only a few mega Pascals and is almost negligible compared to the magnitudes of circumferential stress (σ_θ). A compressive elastic stress of ~ -989 MPa is generated in the circumferential direction (σ_θ) within the YSZ top coat even when the mean lattice misfit strain at the interface is considered zero (Fig. 3(a), case (ii)) for $f = 0.026$. This stress is generated only due to the difference in thermal expansion coefficients of the top coat and the bond coat materials during the cooling process.

The amplitude of circumferential stress at the top coat and bond coat interfaces increased to -1,979 MPa when a mean strain of -0.0057 due to the lattice misfit of $f = 0.0057$ between the top coat and bond coat is included in the model (Fig. 3(b), case (iii)). The 5nm thick ceramic top coat is highly stressed due to this small lattice misfit and under-prediction of film stress by almost 50% is therefore possible if we neglect the effect of lattice misfit. The error may even be higher if the temperature difference is lower and the effect of lattice mismatch strain dominates. However, as the magnitude of the stress is lower than the compressive fracture strength of YSZ (σ_c ~ 4 GPa), this is not expected to cause cracking of the ceramic at the interface immediately after deposition. This compressive strength is calculated using Tabor's rule [51] [that relates hardness to the compressive strength according to $H = C\sigma_c$, where C is the constraint factor with magnitude = 3. The hardness (H) value of 8 mol% YSZ is ~12 GPa [52, 53]. However, the TBC is prone to failure by rupturing of film if subjected to external loading. The top coat is expected to be under compression since the coefficient of thermal expansion of the YSZ ceramic is smaller than that of the bond coat and the substrate. This was experimentally verified within the ceramic top coat by Tanaka et al. [54]. Using micro-Raman spectroscopy, they measured compressive residual stress in the range of ~ -200 MPa in 4 mol% YSZ coating, which was deposited by EB-PVD. Using X-ray diffraction (XRD) and Raman spectroscopy, Teixeira et al. [55], measured compressive residual stress up to -250 MPa in plasma sprayed coatings. The low magnitude of compressive stress may be due to a lower deposition temperature and lower Young's modulus for porous YSZ top coat instead of a much higher 203 GPa modulus used in our model for a fully dense cubic YSZ. Using synchrotron x-ray diffraction Li et al. [56] measured the nonlinear distribution of compressive residual stresses in the range between -200

MPa to -600 MPa within the top coat of a 8 wt% YSZ-NiCrAlY-Hastelloy TBC, and compared the magnitude with their analytical model, which predicted approximately 600 MPa of compressive stress uniformly distributed along the thickness of the top coat. The elastic compressive residual stress counters any applied tensile stresses at the surface or subsurface regions within the top coat and resists crack initiation.

4.3.3 Effect of film thickness

The effect of film thickness on the circumferential stress is shown in Fig. 4 for an initially coherent interface with a lattice misfit of 0.0057. The solid line shows the stress distribution due to the thermal mismatch only, whereas the dashed line demonstrates the combined effect of lattice misfit and thermal mismatch. Clearly the lattice misfit contributes significantly up to a film thickness of 100 nm. Beyond 100 nm, both predictions are almost identical and the effect of lattice misfit on stress is negligible. Dislocations evolve with increasing thickness and reduce the adhesion of the interface. Beyond a thickness of approximately 200 μm, the thin walled pressure vessel assumption breaks down and the stress varies with the radial distance.

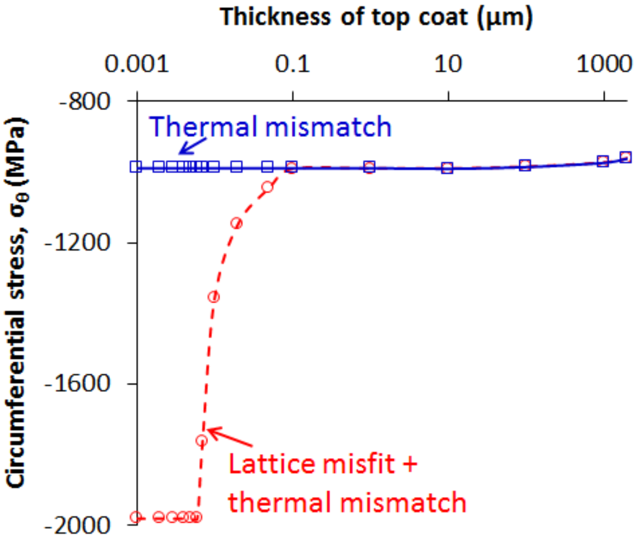

Figure 4 Evolution of thin film stresses with increasing thickness of the film during deposition for $f = 0.0057$. The film is fully coherent up to a thickness of 5 nm. Dislocation nucleation occurs beyond this and stress relaxes to lower value. Only thermal stress remains at the interface beyond a film thickness of approximately 100 nm.

Although lattice misfit does not influence the stress distribution at higher film thickness, it still provides critical information about the interface formation at the beginning of deposition. Depending upon the elastic and physical properties of a material system, the lattice misfit may limit the growth of films during the early stage of deposition. Therefore, consideration of lattice misfit is important for material selection and design for TBCs.

4.3.4 Application of the model to a test case

We now demonstrate how these principles might be applied to the design of a specific application. We consider a cylindrical reaction vessel on the order of 76.2 mm (3 in.) in thickness operating at an internal temperature of 1,200°C and outside temperature requirements not to exceed 90°C (this could be a combustion chamber, gasifier, or furnace). For simplicity, the temperature profile through the TBC layers was determined assuming 1-D steady state heat transfer. The heat transfer coefficient within a reaction chamber containing hot gas and molten slag was taken as ($h_0 = 1{,}000$ W/m^2.K) which is typical at the slag-refractory interface in metallurgical furnaces [57, 58]. The top coat surface temperature is then calculated to be 1,027°C.

The temperature profile at the steady state after the TBC system is heated up to the operating temperature is shown in Figure 5. A temperature reduction of approximately 300°C can be achieved using the 2 mm thick TBC coating. To achieve the desired exterior temperature of 90°C, either a forced cooling system or a much thicker shell will be required. A thicker shell may not be practical for reasons such as manufacturing limitations and weight. To attain sufficient cooling with a 76.2 mm shell would then require a forced cooling system, such as a cooling jacket with a convective heat transfer coefficient of $h_f = 2{,}500$ W/m^2.K. The number is of similar order to that reported by Scholey et al. [58] who estimated a convective heat transfer coefficient of 5200 W/m^2.K based on thermocouple measurements at the steel vessel-water interface of an industrial fuming furnace.

This analysis does not consider any need to reduce temperature at the inner diameter of the shell. For example, if a steel substrate is used for the shell instead of Inconel 738, then a temperature over 700°C is well above the range where the specialty steels used for reactor shells and boiler tubes display acceptable corrosion resistance. For the steels it is necessary to reduce the temperature at the inner, hot surface of the shell by ~ 500°C to 700°C from the gas surface temperature (□ 1000-1200°C). This in turn would require a thermal barrier coating (*cf.* example composition used above) on the order of 4 mm thick. As the residual stresses arising from lattice misfit and thermal mismatch obviate depositing such high thicknesses of YSZ, this approach is currently infeasible.

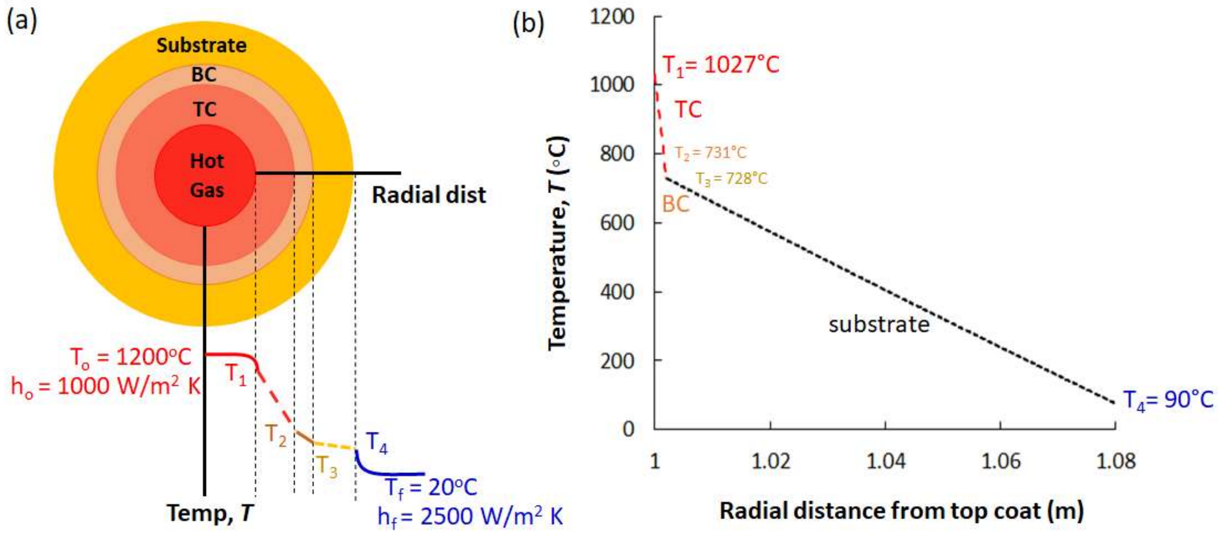

Figure 5 (a) Schematic showing a temperature profile through a TBC system. The coefficient of convective heat transfer inside the reaction chamber was assumed to be 1000 W/m^2.K. (b) The actual temperature profile through the TBC system in our current study. TC and BC represent the top (thermal barrier) coat and bond coat, respectively. The temperature profile within the TGO was assumed to be constant owing to the very thin layer (~ 10 μm).

4.3.5 Residual stress due to TGO formation

In high temperature applications, a thermally grown oxide (TGO) forms between the top coat and the bond coat due to the oxidation of the bond coat in an oxidizing environment. To determine the effect of a TGO layer on the stress profiles, we incorporate a 10 μm thick α-alumina (Al_2O_3) layer at the top coat/bond coat interface. In this model, the interface between top coat and bond coat is assumed to be flat as often observed in TBCs deposited by the EB-PVD process [8].

As described in section 4.1, dislocations will nucleate at the top coat-TGO interface as well as at the TGO-bond coat interface due to high lattice misfits. For simplicity, we assume that the dislocations relieve all the strain due to lattice misfit at those two interfaces and a fully-relaxed semi-coherent interface will exist. High dislocation densities, however, reduce the adhesion across the interfaces [43]. The work of separation for Al_2O_3-Ni interface is reported to be a small fraction of the fracture energy of bulk Ni or bulk Al_2O_3 [42]. During thermal cycling, cracks can easily propagate at the TGO-substrate or TGO-top coat interfaces and are expected to eventually result in brittle interfacial failure.

The thermal stress developed within the layers due to cooling from 1,200°C to 20°C is partially relieved upon heating to the operating temperature as shown in the stress profile in Figs. 6(a) and 6(b)). A moderate magnitude (-464 MPa) of compressive thermal stress remains within the top coat at the operating temperature in the absence of any internal pressure (i.e. $p_0 = 0$ gauge). But if the deposition temperature of the top coat is lower (e.g. 700°C, which is typical for EB-PVD processes), a tensile stress can be generated at the top surface at the operating temperature. Fig.

6(b) shows that a small tensile stress of 36 MPa is predicted when the deposition temperature is 700°C.

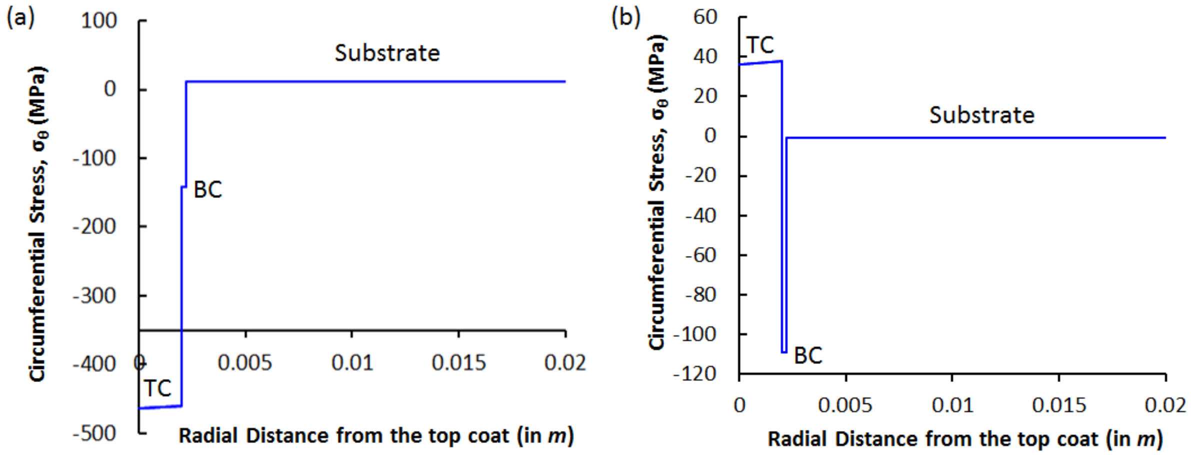

Figure 6 Circumferential stress profile after heating the TBC system to the operating temperature in the absence of any internal pressure (p_0 = 0 MPa gauge). The stress profile for the TBC deposited at (a) 1,200°C and (b) 700°C.

On the other hand, an approximately 190 MPa tensile circumferential stress is developed within the TGO when a constant internal pressure (p_0) of 7.0 MPa is applied at a 1,000°C operating temperature as shown in Figs. 7(a) and 7(b). The magnitude of circumferential stress (190 MPa) within the TGO layer is lower than the tensile strength of Al_2O_3 which is 665 MPa as reported by AZO MATERIALS [59]. The TGO will therefore be only loaded elastically under tension at this operating temperature and pressure. However at temperatures just below a homologous temperature of 0.5, such as would occur under operation at $T \approx 730\,^{\circ}\mathrm{C}$ within the TGO (i.e. T/T_m = 0.43, where T_m is the melting point of α-Al_2O_3 in K), failure of α-Al_2O_3 is expected by cleavage fracture when subjected to a tensile stress of 190 MPa ($\sigma/E \approx 5\times10^{-4}$) [60].

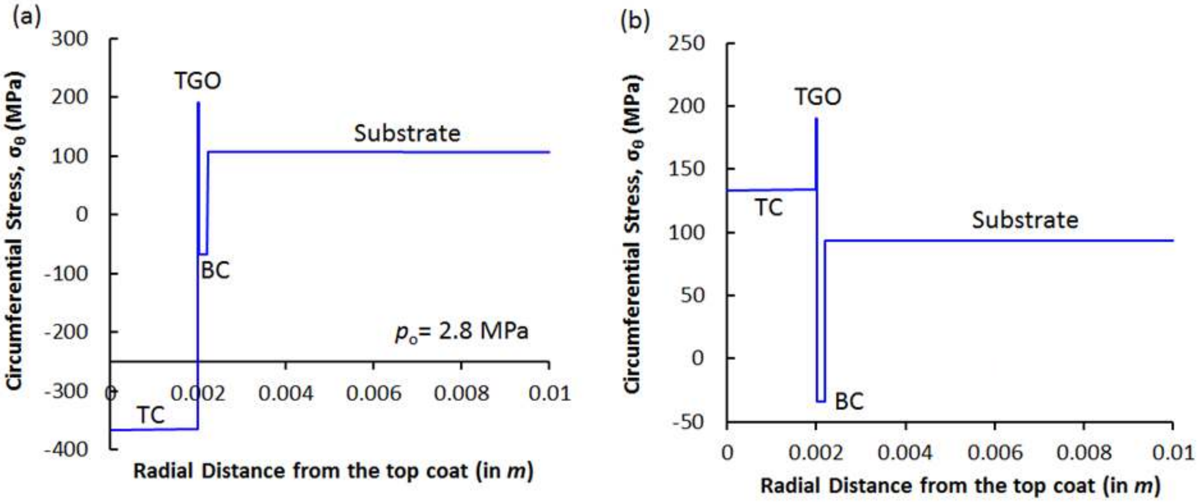

Figure 7 Circumferential stress profile at the operating temperature for a film deposited at (a) 1,200°C and (b) 700°C after 10 μm thick oxide (TGO) formation between the top coat and the bond coat. The pressure, p_0= 7.0 MPa.

Although the stress within the TGO is similar for the profiles shown in Figs. 7(a) and 7(b), the changes in stress at the interface between the top coat (TC), the TGO and the bond coat (BC) are different. For a 1,200°C deposition temperature, the discreet stress difference at the top coat-TGO interface is 557 MPa (-367 MPa to 190 MPa in Fig. 7(a)) at the operating condition. Whereas at the TGO-bond coat interface, the stress difference is 257 MPa (-67 MPa to 190 MPa in Fig. 7(a)). Therefore, at the higher deposition temperature (1,200°C) a sharp change in the magnitude and sign of stress occurs at the top coat-TGO interface (Fig. 7(a)), which might be the location of failure initiation. For a 700°C deposition temperature, the discreet stress difference at the top coat-TGO interface is 57 MPa (133 MPa to 190 MPa in Fig. 7(b)) at the operating condition. Whereas at the TGO-bond coat interface, the stress difference is 224 MPa (-34 MPa to 190 MPa in Fig. 7(b)). Therefore, at the lower deposition temperature (700°C), the change in the magnitude of stress is greater at the TGO-bond coat interface (Fig. 7(b)). In this case, the failure might initiate at the TGO-bond coat interface.

Next we decrease the temperature of the TBC system from the operating temperature to 20ºC to simulate the cooling phase of a single thermal cycle. The internal pressure is reduced to zero gauge ($p_0 = 0$) for the sake of modeling. The corresponding circumferential stress profile developed as a consequence of cooling is shown in Fig. 8(a) and 8(b) for the TBC deposited at 1,200°C and 700°C, respectively. A high compressive stress of ~ -1.06 GPa is generated within the TGO in both cases. Martena et al. [20] predicted compressive stresses of approximately 4 GPa within the TGO layer based on analytical modeling. Using photoluminescence piezospectroscopy, Patel et al. [61] and Guo et al. [62] measured compressive residual stress up to 2.75 GPa and 0.5-2 GPa, respectively, within the TGO. Such high compressive stresses within the thin TGO layer can lead to instability and cracking [63, 64]. Although the magnitude of circumferential stress from our analysis is lower than the compressive strength of the fully dense alumina (> 4 GPa [65]), this amplitude of stress can still initiate micro-cracking in an inadequately dense or porous alumina layer [65]. Furthermore, a tensile stress is generated within the TGO at the operating temperature in the presence of $p_0 = 7.0$ MPa (Figs. 7(a) and 7(b)). Therefore, thermal cycling between 1,000ºC and 20ºC is expected to induce fatigue damage within the TGO due to compression-tension cyclic stressing. Crack initiation may occur within the TGO and at the top coat-TGO and bond coat-TGO interface [66] after a certain number of thermal fatigue cycles to cause the eventual failure of the TBC system.

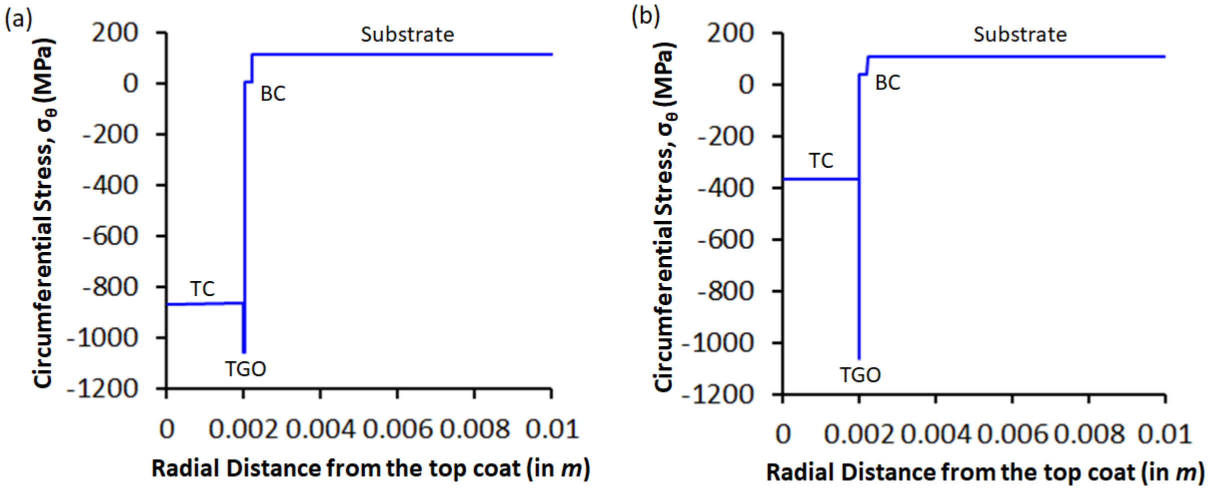

Figure 8 Residual circumferential stress profiles when cooling down the TBC system with a TGO from the operating temperature to 20°C at $p_0 = 0$ gauge for the TBC deposited at (a) 1200°C and (b) 700°C. The TGO is subjected to high compressive stress due to cooling.

The stress difference at the top coat-TGO and TGO-bond coat interfaces changes differently after cooling from the operating temperature to 20°C during thermal cycling for TBCs deposited at 1,200°C and 700°C. Based on the magnitude of the change, the possibility of failure at the interfaces can be predicted. For a 1,200°C deposition temperature, the discreet stress difference at the top coat-TGO interface changes from 557 MPa (-367 MPa to 190 MPa in Fig. 7(a)) at the operating temperature to -188 MPa (-870 MPa to -1058 MPa in Fig. 8(a)) at 20°C after cooling. At the TGO-bond coat interface, however, the stress difference changes from 257 MPa (-67 MPa to 190 MPa in Fig. 7(a)) to -1066 MPa (8 MPa to -1058 MPa in Fig. 8(a)) after cooling to 20°C.

For a 700°C deposition temperature, the discrete stress difference at the top coat-TGO interface changes from 57 MPa (133 MPa to 190 MPa in Fig. 7(b)) at the operating temperature to -688 MPa (-370 MPa to -1058 MPa in Fig. 8(b)) at 20°C after cooling. At the TGO-bond coat interface, on the other hand, the stress difference changes from 224 MPa (-34 MPa to 190 MPa in Fig. 7(b)) to -1099 MPa (41 MPa to -1058 MPa in Fig. 8(b)) after cooling to 20°C. Hence at both the deposition temperatures, the stress-change is comparatively more severe at the TGO-bond coat interface as compared to that at the top coat-TGO interface.

The stress change at the top coat-TGO interface is more pronounced during cooling for the TBC built at a lower deposition temperature than for the TBC built with the higher deposition temperature. Depending upon the relative magnitude of interfacial toughness for these interfaces, the propensity for failure would be expected to reflect this difference..

The variation of thermomechanical stress within the top coat and bond coat due to thermal cycling between the operating temperature (1,000 °C) and room temperature (20°C) is shown schematically in Figs. 9(a-d). As the magnitude of the radial stress component (σ_r) is close to zero, the circumferential stress (σ_θ) is the only significant contributor to the effective Von Mises stress. Therefore, it can be assumed that the TBC is subjected to uniaxial fatigue stress cycles.

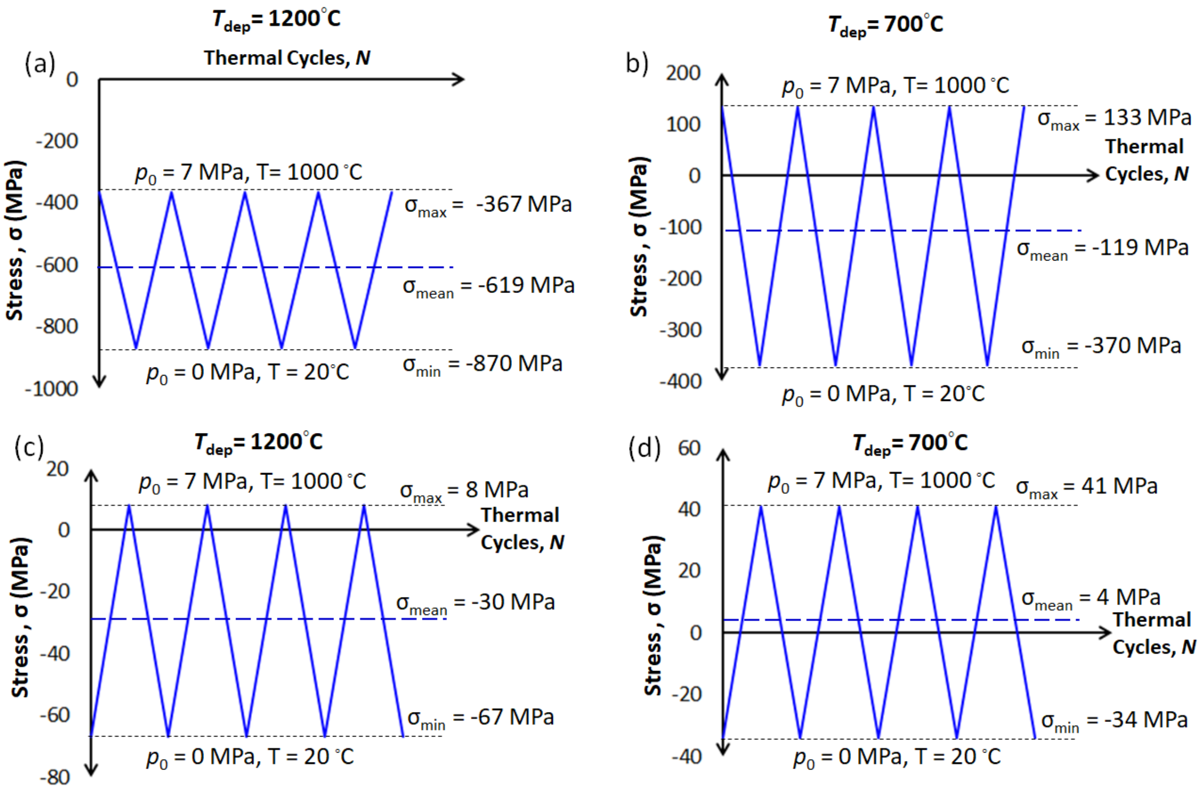

Figure 9 Stress profile within top coat (a-b) and bond coat (c-d) due to thermal cycling between 1,000 °C and 20 °C for TBCs deposited at two different temperatures (T_{dep}) of 1,200 °C (a, c) and 700 °C (b, d).

The deposition temperature (T_{dep}) influences the mean stress $\sigma_{mean} = \left(\sigma_{\max} + \sigma_{\min}\right)/2$ in a fatigue stress cycle although the stress range, $\Delta\sigma = \left(\sigma_{\max} - \sigma_{\min}\right)$ remains the same (Fig. 9(a-d)). The stress range is governed only by the degree of thermal cycling (i.e. the temperature difference between the operating temperature and room temperature) and is independent of the deposition temperature. While the stress-state in the ceramic top coat in a fatigue stress cycle always remains compressive for T_{dep}= 1,200 °C, the stress alters between tension to compression for T_{dep} = 700 °C (Figs. 9(a) and 9(b)). The mean stress in the ceramic top coat is highly compressive ($\sigma_{mean} = -619\,\text{MPa}$) for T_{dep}= 1200 °C, whereas, the magnitude reduces ($\sigma_{mean} = -119\,\text{MPa}$) for T_{dep} = 700 °C. . The stress range for both the deposition temperatures remains ($\Delta\sigma = \left(\sigma_{\max} - \sigma_{\min}\right)$= 503 MPa) Similarly, for the NiCrAlY bond coat; the mean stress changes from compressive ($\sigma_{mean} = -30$ MPa) to tensile ($\sigma_{mean} = 4$ MPa) with a decrease in the deposition temperature, while the stress range ($\Delta\sigma$) is constant at 75 MPa. It is well known that while higher compressive mean stresses increase the fatigue strength and prolong the life of a component, a tensile mean stress reduces the fatigue strength [67]. Therefore, based on a strength-based analysis, a higher deposition temperature is preferred for greater life of the top coat and bond coat for thermal cycling between 1000°C-20°C.

A schematic of the stress state within the TGO layer during the thermal cycling between the operating temperature (1,000°C) and room temperature (20ºC) is shown in Fig. 10. The stress within the TGO depends on the temperature difference in the thermal cycle and the internal pressure. Changing the deposition temperature does not change the stress within the TGO. Hence the profile shown in Fig. 10 might be independent of the deposition temperature. The TGO is subjected to uniaxial compression-tension cyclic loading. The maximum stress ($\sigma_{\max}$ = 190 MPa) in the fatigue cycle is tensile in nature and occurs due to the presence of the 7.0 MPa internal pressure at 1000°C. Due to the cooling, the minimum stress ($\sigma_{\min}$) reduces to - 1058 MPa. Therefore, a compressive mean stress component exists in the fatigue stress cycle as the magnitude of maximum compressive stress is greater than the magnitude of maximum tensile stress.

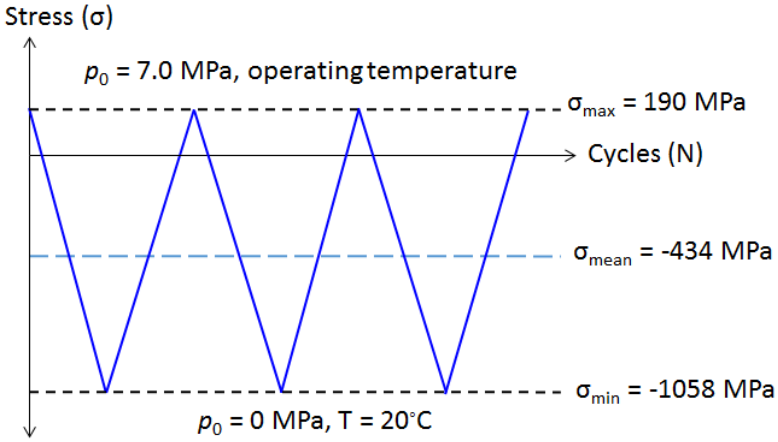

Figure 10 Stress profile within the TGO during thermal cycling between 1000°C and 20°C and internal pressure cycling between 7.0 MPa and zero guage.

During thermal cycling between 1,000°C and 20°C and in the presence of p_0= 7.0 MPa, the cyclic stress range is $\Delta\sigma = \sigma_{\max} - \sigma_{\min} = 190 - (-1058) = 1248$ MPa and the mean stress is $\sigma_{mean} = (\sigma_{\max} + \sigma_{\min})/2$ = - 434 MPa (Fig. 9). The compressive mean stress is beneficial for the life of a component as it reduces the effective cyclic stress amplitude within the material [67, 68]. To understand the effect of an internal pressure on the thermal stress cycle, we compare the magnitudes of the above-mentioned stress range and the mean stress to those in the absence of any internal pressure at the same operating temperature.

In the absence of an internal pressure (i.e., $p_0 = 0$), the maximum stress ($\sigma_{\max}$) within the TGO is zero. Upon cooling to 20°C, the minimum stress $\sigma_{\min}$ within the TGO becomes -1058 MPa. Therefore, in a typical thermal cycle for $p_0 = 0$, the stress in the TGO varies from zero to a negative (compressive) value. For this compression-zero thermal fatigue cycle, the stress range is $\Delta\sigma = \sigma_{\max} - \sigma_{\min} = 0 - (-1058) = 1058$ MPa and the mean stress is $\sigma_{mean} = \left(\sigma_{\max} + \sigma_{\min}\right)/2 =$ -529 MPa. Therefore, the stress-range ($\Delta\sigma$) in a thermal fatigue stress cycle increases and the magnitude of compressive mean stress (σ_{mean}) in that stress cycle decreases in the presence of an internal pressure (p_0). Consequently, the TGO is subjected to more severe cyclic stresses in the presence of an internal pressure. Higher compressive mean stress increases the fatigue life of a component. A non-zero pressure ($p_0 \neq 0$) reduces the magnitude of compressive mean stress within the TGO by shifting the mean stress towards the tensile direction. This will make the TBC more prone to initiating cracks within the TGO and thus failure.

CONCLUSIONS

An analytical model to study stress evolution due to the thermal mismatch and lattice misfit in a multilayered cylindrical TBC system is developed. It is found that the nature of the interface and interfacial stresses depends on the lattice orientation for each layer at the interface as well as the resulting lattice misfit. In the TBC system considered, YSZ-NiCoCrAlY-Inconel 738, compressive stresses on the order of 2 GPa may exist in the cubic YSZ film at the beginning of deposition even for lattice misfits of only 0.0057. The lattice misfit induced stress, however, reduces asymptotically to zero with increasing film thickness and only the thermal stress remains within the TBC layers. At high film thicknesses, the adhesion between the interfaces decreases due to the high defect concentration at the interface and the thermal stress is predicted to drive the failure of the TBC system via interfacial delamination.

When the defect concentration is high at the interface, the adhesion between two adjacent layers decreases when film thickness is high, and thus thermal stress is predicted to drive any failure of the TBC system via interfacial delamination. In the presence of an internal pressure and a high operating temperature, a tensile stress can be generated within the TGO layer which could render the TGO prone to failure via tensile cracking. A comparison between TBCs deposited at two different deposition temperatures revealed that at the operating temperature, the stress difference at the top coat-TGO interface is higher than that at the TGO-bond coat interface for the TBC deposited at the higher temperature. The stress difference, however, is found to be greater at the TGO-bond coat interface for the TBC deposited at lower temperature. The discrete stress drops at the TGO-bond coat, and at the top coat-TGO interfaces may be responsible for interfacial cracking of TBCs deposited at higher and lower temperatures, respectively, during high temperature and pressure operation of the cylindrical reactors.

When the TBC system is subjected to thermal cycling, a high compressive stress on the order of 1.06 GPa was predicted to exist within the TGO during the cooling phase of the cycle. Furthermore, upon cooling to room temperature, the stress difference is always greater at the TGO-bond coat interface than the top coat-TGO interface. Despite that, the magnitude of stress change at the top coat-TGO interface during cooling is significant and is more pronounced for the lower deposition temperature than that at the higher deposition temperature. These findings reveal that the failure of the TBC could occur by delamination at either of the TGO-bond coat or top coat-TGO interfaces when the thickness of the TGO is high enough or even during its growth.

Finally, during a typical thermal cycle in the presence of an internal pressure, the top coat, bond coat and TGO are subjected to a fatigue stress cycle with a compressive mean stress. The magnitude of the stress range is a function of only the operating conditions and remains unchanged with the deposition temperature of the TBC. However, the maximum stress in the top coat and bond coat shifts from compressive to tensile with decreasing the deposition temperature, thereby increasing the expectation for failure by tensile cracking. The mean stress also becomes less compressive, increasing the likelihood of failure by fatigue induced rupture. The presence of internal pressure increases the effective stress range and decreases the magnitude of compressive mean stress within the TGO layer, which is expected to expedite the failure of TBC system by fatigue induced cracking of the TGO.

ACKNOWLEDGEMENTS

This technical effort was performed in support of the National Energy Technology Laboratory's ongoing gasification research, in the Advance Reaction Systems Engineering Program. This research was also supported in part by an appointment to the National Energy Technology Laboratory Research Participation Program, sponsored by the U.S. Department of Energy and administered by the Oak Ridge Institute for Science and Education.

DISCLAIMER

REFERENCES

1. Clarke, D.R., M. Oechsner, and N.P. Padture, *Thermal-barrier coatings for more efficient gas-turbine engines.* MRS Bulletin, 2012. **37**(10): p. 891-898.
2. Wang, C.-L., et al., *Synthesis of Gadolinium Zirconate by Coprecipitaiton and Its Properties for TBC Application.* Key Engineering Materials, 2005. **280-283**: p. 1501-1502.

3. Saini, A.K., D. Das, and M.K. Pathak, *Thermal Barrier Coatings -Applications, Stability and Longevity Aspects.* Procedia Engineering, 2012. **38**: p. 3173-3179.
4. Liu, Z.-G., et al., *Novel thermal barrier coatings based on rare-earth zirconates/YSZ double-ceramic-layer system deposited by plasma spraying.* Journal of Alloys and Compounds, 2015. **647**: p. 438-444.
5. Evans, A.G., et al., *Mechanisms controlling the durability of thermal barrier coatings.* Progress in Materials Science, 2001. **46**(5): p. 505-553.
6. Taylor, R., J.R. Brandon, and P. Morrell, *Microstructure, composition and property relationships of plasma-sprayed thermal barrier coatings.* Surface and Coatings Technology, 1992. **50**(2): p. 141-149.
7. Choi, S.R., J.W. Hutchinson, and A.G. Evans, *Delamination of multilayer thermal barrier coatings.* Mechanics of Materials, 1999. **31**(7): p. 431-447.
8. Vaßen, R., S. Giesen, and D. Stöver, *Lifetime of Plasma-Sprayed Thermal Barrier Coatings: Comparison of Numerical and Experimental Results.* Journal of Thermal Spray Technology, 2009. **18**(5): p. 835.
9. Chen, W.R., et al., *The growth and influence of thermally grown oxide in a thermal barrier coating.* Surface and Coatings Technology, 2006. **201**(3): p. 1074-1079.
10. Lugscheider, E., et al., *Mechanical properties of EB-PVD-thermal barrier coatings by nanoindentation.* Surface and Coatings Technology, 2001. **138**(1): p. 9-13.
11. Wahl, G., et al., *Chemical Vapour Deposition of TBC: An Alternative Process for Gas Turbine Components.* 2000(78576): p. V004T02A015.
12. Padture, N.P., et al., *Towards durable thermal barrier coatings with novel microstructures deposited by solution-precursor plasma spray.* Acta Materialia, 2001. **49**(12): p. 2251-2257.
13. Thompson, J.A. and T.W. Clyne, *The effect of heat treatment on the stiffness of zirconia top coats in plasma-sprayed TBCs.* Acta Materialia, 2001. **49**(9): p. 1565-1575.
14. Aktaa, J., K. Sfar, and D. Munz, *Assessment of TBC systems failure mechanisms using a fracture mechanics approach.* Acta Materialia, 2005. **53**(16): p. 4399-4413.
15. Dong, H., et al., *The influence of temperature gradient across YSZ on thermal cyclic lifetime of plasma-sprayed thermal barrier coatings.* Ceramics International, 2015. **41**(9): p. 11046-11056.
16. Drexler, J.M., et al., *Thermal-gradient testing of thermal barrier coatings under simultaneous attack by molten glassy deposits and its mitigation.* Surface and Coatings Technology, 2010. **204**(16-17): p. 2683-2688.
17. Kumar, V. and K. Balasubramanian, *Progress update on failure mechanisms of advanced thermal barrier coatings: A review.* Progress in Organic Coatings, 2016. **90**: p. 54-82.
18. Kuroda, S., T. Dendo, and S. Kitahara, *Quenching stress in plasma sprayed coatings and its correlation with the deposit microstructure.* Journal of Thermal Spray Technology, 1995. **4**(1): p. 75-84.
19. Kuroda, S. and T.W. Clyne, *The quenching stress in thermally sprayed coatings.* Thin Solid Films, 1991. **200**(1): p. 49-66.
20. Martena, M., et al., *Modelling of TBC system failure: Stress distribution as a function of TGO thickness and thermal expansion mismatch.* Engineering Failure Analysis, 2006. **13**(3): p. 409-426.
21. Neumeier, S., et al., *Lattice Misfit of High Refractory Ruthenium Containing Nickel-Base Superalloys.* Advanced Materials Research, 2011. **278**: p. 60-65.

22. D.A. Porter, K.E.E., *Phase Transformations in Metals and Alloys*. 1st ed. 1984, New York: Chapman and Hall.
23. Nusier, S.Q. and G.M. Newaz, *Growth of interfacial cracks in a TBC/superalloy system due to oxide volume induced internal pressure and thermal loading.* International Journal of Solids and Structures, 2000. **37**(15): p. 2151-2166.
24. Chen, L. and L. Yueming, *Interface stress evolution considering the combined creep–plastic behavior in thermal barrier coatings.* Materials & Design, 2016. **89**: p. 245-254.
25. Abbas, M., L. Guo, and H. Guo, *Evaluation of stress distribution and failure mechanism in lanthanum–titanium–aluminum oxides thermal barrier coatings.* Ceramics International, 2013. **39**(5): p. 5103-5111.
26. Mao, W.G., et al., *Effects of substrate curvature radius, deposition temperature and coating thickness on the residual stress field of cylindrical thermal barrier coatings.* Surface and Coatings Technology, 2011. **205**(8-9): p. 3093-3102.
27. Song, M., Y. Ma, and S.-k. Gong, *Analysis of residual stress distribution along interface asperity of thermal barrier coating system on macro curved surface.* Progress in Natural Science: Materials International, 2011. **21**(3): p. 262-267.
28. Bhattacharyya, A.M., David, *On the Evolution of Stresses due to Lattice Misfit at Metal-Ceramic Interface.* Paper under review in Mater Sci Eng A.
29. Timoshenko SP, G.J., *Theory of Elasticity*. 1970, New York: McGraw Hill.
30. Mazur, Z., et al., *Failure analysis of a gas turbine blade made of Inconel 738LC alloy.* Engineering Failure Analysis, 2005. **12**(3): p. 474-486.
31. Quadakkers, W.J., et al., *Oxidation characteristics of a platinized MCrAlY bond coat for TBC systems during cyclic oxidation at 1000 °C.* Surface and Coatings Technology, 2005. **199**(1): p. 77-82.
32. Gadag, S., G. Subbarayan, and W. Barker, *Thermo-elastic properties of dense YSZ and porous Ni-ZrO2 monolithic and isotropic materials.* Journal of Materials Science, 2006. **41**(4): p. 1221-1232.
33. Lucht, e.a., *Precise Measurement of the Lattice Parameters of*
Sapphire in the Temperature Range 4.5 K - 250 K Using
the M¨ ossbauer Wavelength Standard. J. Appl. Cryst, 2003. **36**(Part 4): p. 1075-1081.
34. Pomfret, M., *An Investigation of Solid Oxide Fuel Cell Chemistry: A Spectroscopic Approach*, in *Chemistry and Biochemistry*. 2007, University of Maryland: College Park, MD. p. 221.
35. Mercier, D., *Oxidation Behavior of Nanostructured CoNiCrAlY and*
NiCoCrAlY Sprayed by HVOF, in *Department of Mining and Materials Engineering*. 2010, McGill University: Montreal, Canada. p. 88.
36. Korte, C., et al., *Ionic conductivity and activation energy for oxygen ion transport in superlattices-the semicoherent multilayer system YSZ (ZrO2 + 9.5 mol% Y2O3)/Y2O3.* Physical Chemistry Chemical Physics, 2008. **10**(31): p. 4623-4635.
37. Wunderlich, W., *The Atomistic Structure of Metal/Ceramic Interfaces Is the Key Issue for Developing Better Properties.* Metals, 2014. **4**(3): p. 410.
38. Kikuchi, A., *Calculation of Misfit-Dislocation Density Generated by Lattice Mismatch at the NiSi2–Si Interface.* physica status solidi (b), 1997. **203**(1): p. 79-86.
39. Atkinson, A. and S.C. Jain, *The energy of systems of misfit dislocations in epitaxial strained layers.* Thin Solid Films, 1992. **222**(1): p. 161-165.

40. Sasaki, T., et al., *Atomic and Electronic Structures of Ni/YSZ(111) Interface.* MATERIALS TRANSACTIONS, 2004. **45**(7): p. 2137-2143.
41. Christensen, A. and E.A. Carter, *Adhesion of ultrathin ZrO2(111) films on Ni(111) from first principles.* The Journal of Chemical Physics, 2001. **114**(13): p. 5816-5831.
42. Zhang, W., J.R. Smith, and A.G. Evans, *The connection between ab initio calculations and interface adhesion measurements on metal/oxide systems: Ni/Al2O3 and Cu/Al2O3.* Acta Materialia, 2002. **50**(15): p. 3803-3816.
43. Linghu, Y., et al., *The Adhesive Properties of Coherent and Semicoherent NiAl/V Interfaces Within the Peierls-Nabarro Model.* Crystals, 2016. **6**(4): p. 32.
44. Stollberg, D.W., et al., *Nanoindentation measurements of combustion CVD Al2O3 and YSZ films.* Materials Science and Engineering: A, 2003. **359**(1–2): p. 112-118.
45. - *Laser CVD Process for High Speed Deposition of YSZ Films.* - Materials Science Forum: p. - 1213.
46. Bouzakis, K.D., et al., *Determination of mechanical properties of electron beam-physical vapor deposition-thermal barrier coatings (EB-PVD-TBCs) by means of nanoindentation and impact testing.* Surface and Coatings Technology, 2003. **163–164**: p. 75-80.
47. Park, S.H., et al., *Indentation on YSZ thermal barrier coating layers deposited by electron beam PVD.* Philosophical Magazine, 2006. **86**(33-35): p. 5453-5463.
48. Kondoh, J., et al., *Yttria concentration dependence of tensile strength in yttria-stabilized zirconia.* Journal of Alloys and Compounds, 2004. **365**(1): p. 253-258.
49. Poklad, A., et al., *Orientation Relationship between the TRIP Steel Substrate and the ZrO2 thin Film.* steel research international, 2011. **82**(9): p. 985-989.
50. Sillassen, M., et al., *Low-Temperature Superionic Conductivity in Strained Yttria-Stabilized Zirconia.* Advanced Functional Materials, 2010. **20**(13): p. 2071-2076.
51. Tabor, D., *The hardness of solids.* Review of Physics in Technology, 1970. **1**(3): p. 145.
52. Chen, T., et al., *Phase stability, microstructural evolution and room temperature mechanical properties of TiO2 doped 8mol% Y2O3 stabilized ZrO2 (8Y-CSZ).* Ceramics International, 2008. **34**(2): p. 365-370.
53. Aruna, S.T., N. Balaji, and K.S. Rajam, *Phase transformation and wear studies of plasma sprayed yttria stabilized zirconia coatings containing various mol% of yttria.* Materials Characterization, 2011. **62**(7): p. 697-705.
54. Tanaka, M., et al., *Residual stress measurement of an EB-PVD Y2O3-ZrO2 thermal barrier coating by micro-Raman spectroscopy.* Surface and Coatings Technology, 2009. **204**(5): p. 657-660.
55. Teixeira, V., et al., *Effects of deposition temperature and thermal cycling on residual stress state in zirconia-based thermal barrier coatings.* Surface and Coatings Technology, 1999. **120–121**: p. 103-111.
56. Li, C., et al., *Understanding the residual stress distribution through the thickness of atmosphere plasma sprayed (APS) thermal barrier coatings (TBCs) by high energy synchrotron XRD; digital image correlation (DIC) and image based modelling.* Acta Materialia, 2017. **132**: p. 1-12.
57. Utigard, T.A., A. Warczok, and P. Desclaux, *The measurement of the heat-transfer coefficient between high-temperature liquids and solid surfaces.* Metallurgical and Materials Transactions B, 1994. **25**(1): p. 43-51.

58. Scholey, K.E., G.G. Richards, and I.V. Samarasekera, *Heat-transfer phenomena in water-cooled zinc-fuming furnace jackets.* Metallurgical Transactions B, 1991. **22**(2): p. 163-175.
59. http://www.azom.com/properties.aspx?ArticleID=52, *Alumina Aluminium Oxide Al2O3 a Refractory Ceramic Oxide.*
60. Ashby, M.F.a.T., B. *Micromechanisms of fracture and elevated temperature fracture mechanics*. Mechanical behaviour of materials 1980; pp.47-89].
61. Patel, N.V., *Use of Thermally Grown Oxide Stress Measurements to Predict Remaining Life of Thermal Barrier Coatings under Realistic Turbine Engine Conditions.* 2014.
62. Guo, S. and Y. Kagawa, *Young's moduli of zirconia top-coat and thermally grown oxide in a plasma-sprayed thermal barrier coating system.* Scripta Materialia, 2004. **50**(11): p. 1401-1406.
63. Evans, A.G., J.W. Hutchinson, and M.Y. He, *Micromechanics model for the detachment of residually compressed brittle films and coatings.* Acta Materialia, 1999. **47**(5): p. 1513-1522.
64. Cheng, J., et al., *Thermal/residual stress in an electron beam physical vapor deposited thermal barrier coating system.* Acta Materialia, 1998. **46**(16): p. 5839-5850.
65. Auerkari, P., *Mechanical and physical properties of engineering alumina ceramics*. 1996: Technical Research Centre of Finland Finland.
66. Hutchinson, J.W. and A.G. Evans, *On the delamination of thermal barrier coatings in a thermal gradient.* Surface and Coatings Technology, 2002. **149**(2–3): p. 179-184.
67. Bhattacharyya, A., et al., *Cyclic Constitutive Response and Effective S–N Diagram of M50 NiL Case-Hardened Bearing Steel Subjected to Rolling Contact Fatigue.* Journal of Tribology, 2015. **137**(4): p. 041102-041102-15.
68. Bhattacharyya, A., et al., *Influence of Residual Stress and Temperature on the Cyclic Hardening Response of M50 High-Strength Bearing Steel Subjected to Rolling Contact Fatigue.* Journal of Engineering Materials and Technology, 2016. **138**(2): p. 021003-021003-14.